Can ultrasound attenuation measurement be used to characterise grain statistics in castings? ⋆

Yuan Liu[a,*], Michał K. Kalkowski[a], Ming Huang[a], Michael J. S. Lowe[a], Vykintas Samaitis[b], Vaidotas Cicėnas[b], Andreas Schumm[c]

[a] *Department of Mechanical Engineering, Imperial College London, Exhibition Road, London SW7 2AZ, United Kingdom*
[b] *Prof. K.Baršauskas Ultrasound Research Institute, Kaunas University of Technology, K. Baršausko st. 59, Kaunas 51423, Lithuania*
[c] *EDF Lab Les Renardières, EDF R&D, Avenue des Renardières, 77818 Moret-sur-Loing, France*

Abstract

Industrial inspection protocols are qualified using mock-ups manufactured according to the same procedure as the plant part. For coarse-grained castings, known for their low inspectability, relying on mock-ups becomes particularly challenging owing to the variability of grain properties among components. Consequently, there is a keen interest in the capability to verify whether the grain size of the component under test matches the qualification specification in-situ. This paper investigates the potential of an attenuation measurement for assessing the ultrasonic inspectability of coarse-grained components using qualified procedures in a practical setting. The experimental part of the study focuses on an industrial Inconel 600 mock-up with spatially varying attenuation, measured across the entire sample in an immersion tank. Three zones with distinctly different attenuations were examined using metallography, which allowed for calculating classical grain size histograms and two-point correlation functions. For one of the zones, we synthesised the microstructure with the same statistical properties numerically and simulated the propagation of ultrasound using a grain-scale finite element model. The results showed good agreement with the experiment, and lead to several suggestions for the reasons for the discrepancy, the varying grain size statistics being the most likely. A parametric study, which followed, depicted the effect of the mean and standard deviation-to-mean ratio of the log-normal grain size distribution on the attenuation of ultrasound and its frequency dependence. Most notably, we demonstrated the known non-uniqueness of the relationship between the log-normal grain size distribution parameters and the attenuation. We suggested that the correlation length calculated from a single exponential fit to the two-point correlation function is a more robust metric describing grain statistics for this context, which can be obtained from attenuation. The correlation lengths estimated from measured attenuation using the second-order approximation model for the three zones of the studied mock-up yielded results of acceptable accuracy. We concluded that this metric could replace the average grain size in practical settings, as it retains more statistical information than the mean grain size and allows for linking measurements to the established theoretical attenuation models which this paper demonstrates.

Keywords: polycrystalline materials, material characterisation, ultrasound attenuation, grain size distribution

1. Introduction

Non-destructive evaluation (NDE) of nuclear power plant (NPP) components to detect defects such as cracks is critical for their safety. National regulators require the owners of NPPs to demonstrate their

⋆This manuscript version is made available under the CC-BY-NC-ND 4.0 license
*Corresponding author
Email address: y.liu14@imperial.ic.uk (Yuan Liu)

Manuscript accepted for publication in Ultrasonics (115), August 2021, 106441, DOI on 29 Jan, 2021

inspection capability for safety-critical components to rule out potential faults that might occur. Each type of a defect for an individual part typically needs a specific, qualified procedure for inspection, which ensures that it can be detected when larger than a particular threshold size. The components of NPPs can then be described with inspectability indices, determining the type and size of defects which can be identified with given qualified procedures. One of the key challenges in ultrasonic testing is the detection of cracks and inclusions in thick cast austenitic steel or nickel alloy components because the ultrasound suffers from scattering from the large grains in these materials.

An essential aspect of inspection procedure qualification is the demonstration that the claimed inspection depth is obtained. This depth is limited by the signal-to-noise ratio (SNR), governed by the interactions between the ultrasound and the grain structure. The loss of amplitude caused by scattering-related attenuation and the strength of reflection from a postulated defect determine the signal part of the SNR. In the pulse-echo arrangement, the noise part comes from the backscatter of the signal from grain boundaries along the path. This paper is concerned with the 'signal' element of the SNR. Our interest is in the attenuation of the ultrasound as it propagates through polycrystalline materials.

Qualifications rely on mock-ups which are manufactured using the same procedure as the component of interest. However, owing to the complexity of the solidification process, which cannot be fully controlled, the correspondence between the mock-up castings and the cast components on-site cannot always be guaranteed. Site operators would benefit from an ultrasonic measurement that could indicate whether or not a section of a component has similar grain properties to the mock-up used for procedure qualification. From the viewpoint of the operators of NPPs, two aspects are of interest in this context. First, is it possible to obtain a useful, even if somewhat simplistic, metric describing the grain size (or its distribution) from attenuation measurements? Second, can the theoretical attenuation models be readily applied to industrial cases to inform the design of the inspection procedures? In reality, grain properties of castings are incredibly variable, even from location to location within a single component. This presents a challenge for inspection qualification, which needs to cover a typical range of sizes and distributions for a given component. While it is a common intuition in the community that backscatter offers a better starting point for grain-size inversion, the simplicity of the attenuation measurement makes it still a preferred choice for the industry. Furthermore, it gives direct information about the distance of propagation that can be expected during the inspection on the plant.

A majority of publications to date, which will be reviewed in the following paragraphs, addressed the problem from a purely theoretical perspective, using mathematically convenient grain structure distributions and rarely modelling the propagation of ultrasound explicitly. However, they provided invaluable insights, which found the current understanding of ultrasound propagation in polycrystals and are essential to the investigation presented in this paper. The extensive studies on the scattering-induced attenuation originated from the formulation of the three attenuation regimes – Rayleigh [1], stochastic [2] and geometric regimes [3, 4] – and the power-law relationships between attenuation and grain size, shown in Eq. (1),

$$\begin{aligned} \alpha_{\mathrm{R}} &\propto D^3 f^4 \qquad & \lambda D^{-1} &\gg 1 \\ \alpha_{\mathrm{s}} &\propto D^1 f^2 \qquad & \lambda D^{-1} &\approx 1 \\ \alpha_{\mathrm{g}} &\propto D^{-1} f^0 \qquad & \lambda D^{-1} &\ll 1, \end{aligned} \tag{1}$$

where the subscripts R, s and g denote the Rayleigh, stochastic and geometric regimes, respectively, α, D, f and λ represent the attenuation coefficient, grain size, frequency and wavelength.

Early studies on the effect of the statistical distribution of grain size on attenuation were frequently based on the Roney's theoretical model [5], which relates the grain diameter to the attenuation directly. Smith incorporated the grain size distribution into the Roney's model and found that two specimens with the same mean grain size but different distributions could have significantly different frequency dependence of attenuation [6]. Nicoletti and Anderson proposed a deconvolution method to obtain the grain size distribution from the attenuation [7].

More recent studies on this topic use the Unified Theory [8] and Weaver's model [9], which describe grain size with a two-point correlation function (TPCF). The TPCF shows the possibility of two randomly picked

points locating in the same grain [10]. It is often approximated with an exponential $\exp(-r/a)$, where a is called the linear correlation length. Therefore, to discuss the effect of the grain size distribution on the attenuation, it is required to relate the grain size distribution to the TPCF. Suppose the attenuation of a sample or a numerical model with a certain distribution is to be calculated. In that case, the TPCF can be directly measured experimentally [11] or numerically [12–18] and an analytical fit can be applied to the theoretical models. If the TPCF cannot be measured, for example, in a purely theoretical calculation, a relationship between the volumetric statistics and TPCF needs to be assumed, so that the attenuation can be directly expressed and solved using the volumetric statistics [19–21].

Ryzy et al. studied the influence of grain morphology on ultrasonic attenuation in polycrystalline materials [13]. The TPCFs were directly measured from the three-dimensional (3D) finite element (FE) models and the polynomial fits were used in the Weaver's model. Good agreement was achieved when comparing the numerical and semi-analytical results. The results showed that the grain uniformity has a big impact on the P-wave attenuation in the Rayleigh-stochastic transition region, where an oscillatory behaviour was observed. Norouzian et al. used Dream.3D [22] to create representative polycrystalline models with log-normal grain size distributions [16]. The attenuation was calculated theoretically using the synthetic volumes [15]. They found that the frequency dependence of attenuation was strongly affected by the width of the distribution and that the correlation between attenuation and the width of the distribution could be modelled with a power law, considering only one mean grain size and single frequency.

Arguelles and Turner incorporated the description of the grain size distribution in a theoretical solution based on the Weaver's model [9] by using a log-normal distribution of correlation lengths. They found that the grain size distribution had a measurable effect on attenuation and a wide distribution of grain size reduced the frequency dependence order [19]. Bai et al. validated this model experimentally [23]. Sha presented an explicit form of TPCF for a polycrystal with uniform equiaxed grains [20]. Analytical solutions of attenuation and scattering coefficients were derived with the proposed TPCF, enabling the attenuation and scattering to be calculated with the volumetric grain size. Sha extended this research to polycrystalline materials with statistically equiaxed grains [21]. By using the grain distribution data – grain statistics and TPCF – from the 3D FE models from Ryzy's work [13], this relationship was validated. The analytical attenuation model for the longitudinal wave was verified by comparing with the 3D FE results given by Ryzy et al. [13].

Although the studies described above have shown that the distribution of grain size has a measurable effect on attenuation, they mostly discussed theoretical configurations. Our work is motivated by the industrial interest in determining the capabilities and limitations of the attenuation measurement for obtaining the volumetric statistics of grains. The investigation is based on a component of industrial relevance, but with relatively little complexity from the NPP operator's perspective. We combine the material examinations and attenuation measurements on an Inconel 600 casting mock-up with numerical and analytical simulations. While most of the existing studies on the effect of the grain size distribution on the attenuation rely on the theoretical models, we used the second-order approximation [17] (of the Unified Theory [8] type) alongside grain-scale 3D finite element modelling, which simulated the ultrasound in the time domain directly. The profound advantage of the latter, exploited and validated in several recent papers, e.g. [14, 24, 25], is that it can solve the full-physics scattering problem without major assumptions adopted in the theoretical models.

We intend to evaluate the potential for knowledge transfer between highly theoretical modelling and NDE practitioners and provide insights into establishing inspectability metrics based on longitudinal wave attenuation in castings. The paper concludes with a demonstration of the inversion results and practical implications of our findings. The remaining sections report the subsequent stages of our investigation. In Section 2, we present the mock-up, together with measured microstructure characteristics and longitudinal wave attenuation; the spatial variation of the grain statistics and the extent of the uncertainty are also discussed. Section 3 introduces the FE models used in this paper, of which a convergence study is reported in Appendix A. We show how the 3D microstructure is synthesised from the measured metallography of the sample and compare the attenuation predicted using FE with the measured one. Motivated by the spatial variation of the grain statistics, in Section 4 we present a parametric study revealing the effect of grain size distribution on attenuation and its dependence on frequency, mean and standard deviation-to-mean ratio of the distribution. Section 5 offers the final demonstration and a discussion about leveraging attenuation

measurements for determining grain size using the second-order approximation model in the context of the studied mock-up. Finally, the conclusions are given in Section 6.

2. The mock-up: an Inconel 600 casting

2.1. Description

The mock-up (EDF reference 1591-B359-D3) is one out of six sections with about 135 mm diameter and 100 mm height which were cut out of a cylindrical cast Inconel 600 slab. The sections underwent heat treatment with the effect of increasing grain size through the merging of smaller grains during the heating and subsequent annealing cycle. This series of mock-ups was intended to serve as laboratory mock-ups to evaluate backscatter and attenuation of ultrasonic waves. According to the manufacturing procedure and previous measurements at EDF's laboratories, the mock-up is assumed to be homogeneous in a macroscopic sense, with approximately equiaxed grains and no texture. Further, it does not exhibit a layered structure with different grain sizes. A photograph of the specimen is shown in Fig. 1.

2.2. Attenuation measurements

The attenuation across the sample described in the previous subsection was measured experimentally. For the sake of better accuracy and confidence in the results, the measurements were taken in an immersion tank using two configurations: pulse-echo (PE) and through-transmission (TT). In practice, the through-transmission setup can be treated as the more reliable approach, as it is less affected by the geometry and the uneven surface of the mock-up than a pulse-echo technique. In this section, the measurements for both PE and TT approaches are presented and compared, however, in the subsequent sections, we only use the data from the PE measurement, as it is more representative of a real in-situ scenario.

A schematic diagram of the measurement set-up is shown in Fig. 1. For pulse-echo measurements, the transducer T_1 (Olympus C326-SU) was used to collect signals reflected from front-wall ($P_{r_1}(t)$) and back-wall ($P_{r_2}(t)$) of the mock-up. In the through-transmission approach, another sensor T_2, with same model and characteristics as T_1, was introduced to collect the water path signal without the presence of the specimen ($P_w(t)$) and the signal propagated through the mock-up ($P_{t_1}(t)$). In both cases, the transducers were scanned across the *x-y* plane with the scan step of 1 mm covering the entire volume of the specimen. The transducers T_1 and T_2 were 9.53 mm flat face probes operating at the frequency of 5 MHz with the bandwidth of 56.33% at −6 dB level. The height of the water column between the transducer T_1 and the specimen (d_1) was 85 mm. The water path between transducers T_1 and T_2 in the absence of the specimen (d) was 227 mm. These positions were deliberately selected to position the mock-up in the far-field (the near-field was within 19.6 mm) and to avoid the overlap of the reflected and transmitted signals in the time domain. The data acquisition was carried out with an ultrasonic immersion scanner (TecScan, Canada) with a sampling frequency of 200 MHz.

After the acquisition, the frequency-dependent attenuation was calculated at each scanning position. The material properties of both the mock-up and water were assumed for subsequent calculations, as follows: c_s=5800 m s^{-1}; ρ_s=8290 kg m^{-3}; c_w=1482 m s^{-1}; ρ_w=1000 kg m^{-3}. For the pulse-echo measurement, the attenuation coefficient was calculated from the front-wall and back-wall reflected signal amplitude spectra [26]:

$$|U_{r_1}(f)| = \left|U_0(f)R_{w_s}\right| \exp\left[-2\alpha_w(f)d_1\right], \tag{2}$$

$$\left|U_{r_2}(f)\right| = \left|U_0(f)(-R_{w_s})T\right| \exp\left[-2\alpha_w(f)d_1 - 2\alpha(f)L\right], \tag{3}$$

where $U_{r_1}(f)$ and $U_{r_2}(f)$ are the Fourier transforms of the measured time histories $P_{r_1}(t)$ and $P_{r_2}(t)$, $U_0(f)$ is the Fourier transform of the initial pulse $P_0(t)$ launched by transducer, f is frequency, R_{w_s} is the reflection coefficient at the water-specimen interface, $\alpha_w(f)$ is the attenuation in water, d_1 is the distance between

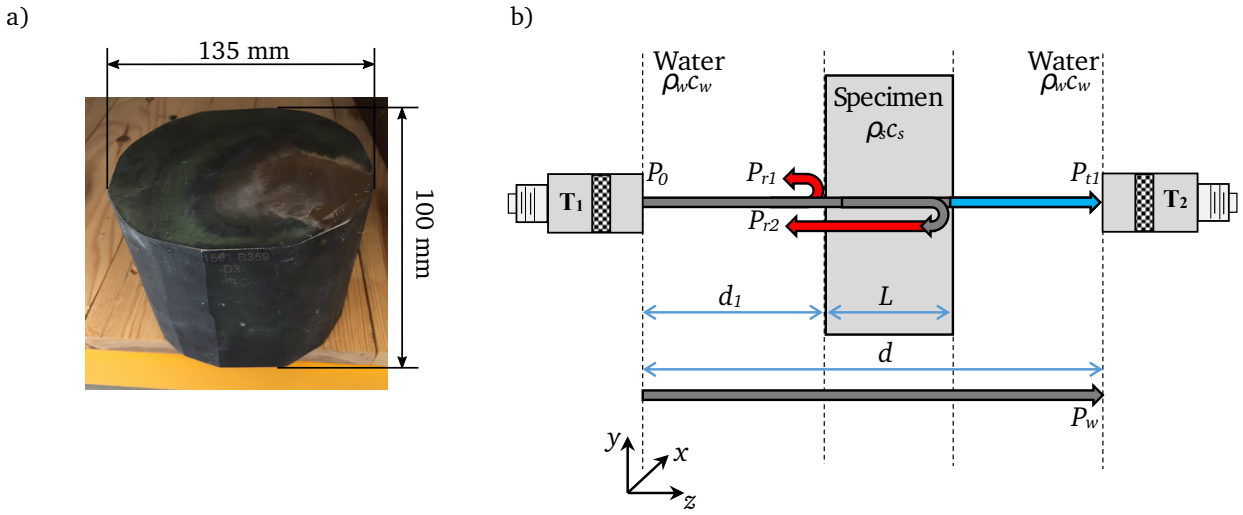

Figure 1: The Inconel 600 mock-up: (a) a photograph of the sample; (b) attenuation measurement setup with the arrangements for PE and TT measurements.

the transducer and the specimen, T is the transmission coefficient, $\alpha(f)$ is the attenuation in the specimen, and L is the thickness of the specimen. The reflection coefficient R_{w_s} is defined as:

$$R_{w_s} = \frac{z_s - z_w}{z_s + z_w}, \tag{4}$$

where the water and specimen characteristic acoustic impedances are $z_w = \rho_w c_w$ and $z_s = \rho_s c_s$, respectively. The transmission coefficient T represents the loss of amplitude when propagating across both the water-specimen and the specimen-water interfaces:

$$T = \frac{4 z_s z_w}{(z_s + z_w)^2}, \tag{5}$$

where we note that $T = 1 - R_{w_s}^2$.

In the case of the through-transmission measurement, the attenuation coefficient was obtained from the signal transmitted through the water without the specimen, $P_w(t)$, and the signal transmitted through the immersed specimen, $P_{t_1}(t)$. The Fourier transforms of the respective signals can be written as [26]:

$$\left|U_{t_1}(f)\right| = |U_0(f) T| \exp\left[-\alpha_w(f)(d - L) - \alpha(f) L\right], \tag{6}$$

$$|U_w(f)| = |U_0(f)| \exp\left[-\alpha_w(f) d\right], \tag{7}$$

where d is the distance between the transducers, $U_{t_1}(f)$ and $U_w(f)$ are the Fourier transforms of the measured time histories $P_{t_1}(t)$ and $P_w(t)$. To achieve high accuracy with finite size transducers, the diffraction correction must be applied. This was done following [27]:

$$D_i(f) = 1 - \exp\left[-\jmath \frac{2\pi}{s_i(f)}\right] \left\{ J_0\left[\frac{2\pi}{s_i(f)}\right] + \jmath J_1\left[\frac{2\pi}{s_i(f)}\right] \right\}, \tag{8}$$

where $\jmath$ is the imaginary unit, J_0, J_1 are the Bessel function of the 0^{th} and the 1^{st} order, respectively, and the subscript i indicates the wave path. The arrangements considered in this paper are governed by four different wave paths (referring to Fig. 1), so four s_i parameters ($s_i = 2\pi z/(kr^2)$; refer to [27]) are needed:

$$s_{r_1}(f) = \frac{2 d_1 c_w}{f r^2}, \tag{9}$$

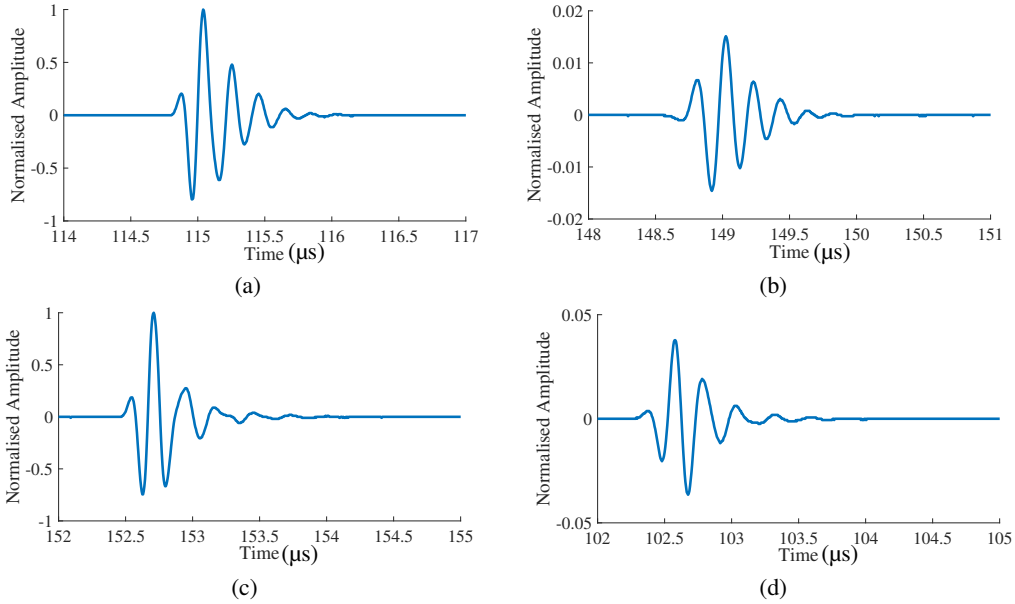

Figure 2: Time histories measured at the centre of the mock-up: (a) front-wall reflection P_{r_1}, (b) back-wall reflection P_{r_2}, (c) water path signal P_w, (d) signal transmitted through the sample P_{t_1}.

$$s_{r_2}(f) = \frac{2d_1 c_w}{fr^2} + \frac{2Lc_s(f)}{fr^2}, \tag{10}$$

$$s_w(f) = \frac{dc_w}{fr^2}, \tag{11}$$

$$s_{t_1}(f) = \frac{(d-L)c_w}{fr^2} + \frac{Lc_s(f)}{fr^2}, \tag{12}$$

where r is the active radius of the transducer.

The attenuation coefficients for both measurement configurations were calculated from the reflected and transmitted signals, and including the correction factors outlined above, using the following expressions:

$$\alpha_{\mathrm{PE}}(f) = \frac{1}{2L}\left[\ln\left(\frac{|U_{r_1}(f)|}{|U_{r_2}(f)|}\right) - \ln\left(\frac{|D_{r_1}(f)|}{|D_{r_2}(f)|}\right) + \ln\left(\left|1 - R_{w_s}^2\right|\right)\right], \tag{13}$$

$$\alpha_{\mathrm{TT}}(f) = \frac{1}{L}\left[\ln\left(\frac{|U_w(f)|}{|U_{t_1}(f)|}\right) - \ln\left(\frac{|D_w(f)|}{|D_{t_1}(f)|}\right) + \ln\left(\left|1 - R_{w_s}^2\right|\right)\right]. \tag{14}$$

An example of the raw signals at the central point of the mock-up collected in the pulse-echo arrangement is presented in Fig. 2(a) and (b). Fig. 2(a) shows front-wall reflection P_{r_1}, while Fig. 2(b) corresponds to the back-wall reflection P_{r_2}. The signals are normalised by the former. In the same fashion, Fig. 2(c) and (d) shows the water path signal P_w and the transmission signal P_{t_1} collected using the through-transmission setup, normalised with respect to the water path signal.

The results presented above suggest that the bandwidth of the signal is 2.5 MHz (3.5–6 MHz) at −6 dB. This bandwidth should be used for evaluation of attenuation coefficients, as it provides most of the signal energy. The example of the frequency-dependent attenuation at the central point of the mock-up with coordinates (x=72 mm, y=41 mm) can be seen in Fig. 3. Around the central frequency of the obtained signals (4.5 MHz), there is good agreement between both methods. The discrepancies at frequencies higher than 6 MHz and lower than 3.5 MHz can be attributed to low signal energy beyond the −6 dB bandwidth. The comparison between the PE and TT methods indicates that despite the former being more affected by uncertainties (positioning, the effect of the surface of the specimen), the difference within the transducer's bandwidth is practically negligible. What is more important, the PE setup better represents an in-situ scenario.

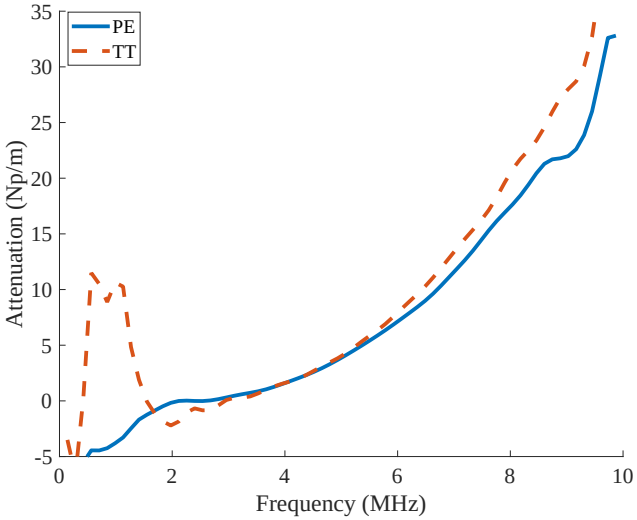

Figure 3: Frequency-dependent attenuation at the central point of mock-up calculated from both the pulse-echo and the through-transmission measurements.

Maps of attenuation coefficients $\alpha_{\mathrm{PE}}(f)$ and $\alpha_{\mathrm{TT}}(f)$ at f=5 MHz are presented in Fig. 4. On the left-hand side of each map, the footprints of three flat-bottomed holes, purposely manufactured in the mock-up, can be observed. Three areas corresponding to distinctly different attenuation levels were identified from the attenuation map. The zones are referred to as 'Zone 1', 'Zone 2' and 'Zone 3' and their locations are marked in Fig. 4. The circles around each zone show the footprint of the probe at each scanning position. The subsequent sections of this paper use a single PE attenuation curve for each zone (taken at the centre of the circles in Fig. 4: (x_1=73 mm, y_1=47 mm) - Zone 1; (x_2=95 mm, y_2=87 mm) - Zone 2; (x_3=105 mm, y_3=47 mm) - Zone 3). To demonstrate the range of attenuation in the specimen, we plotted the results for all points within the rectangular area marked in Fig. 4(a), overlaid with the curves corresponding to the centres of the chosen zones defined above, in Fig. 5, where the curves close to the upper bound were measured close to the mock-up edge so are affected by the edge reflections.

2.3. Targeted examination

The ground truth grain properties for the three zones under investigation were obtained from material examination. The metallographic analysis was carried out by first polishing the surface to be analysed with increasingly fine sanding paper, then immersing the part for a certain time in *aqua regia*, a concentrated mixture of nictric and hydrochloric acids. This acid attack reveals the grain structure, which would then be investigated under a microscope, if the part was small enough. In our case, a thin layer of liquid plastic was applied on the three regions, which was removed after solidification and subsequently analysed. This

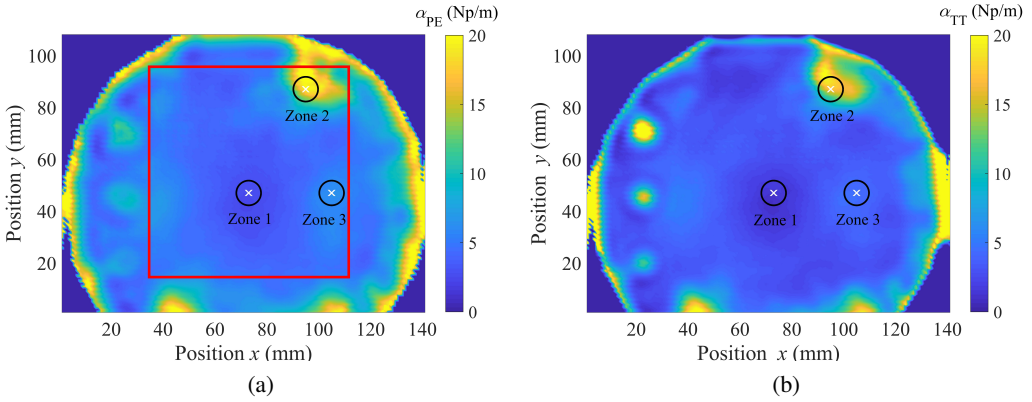

Figure 4: Attenuation coefficients (a) $\alpha_{\mathrm{PE}}(f)$ and (b) $\alpha_{\mathrm{TT}}(f)$ at the central frequency (5 MHz) of the probe.

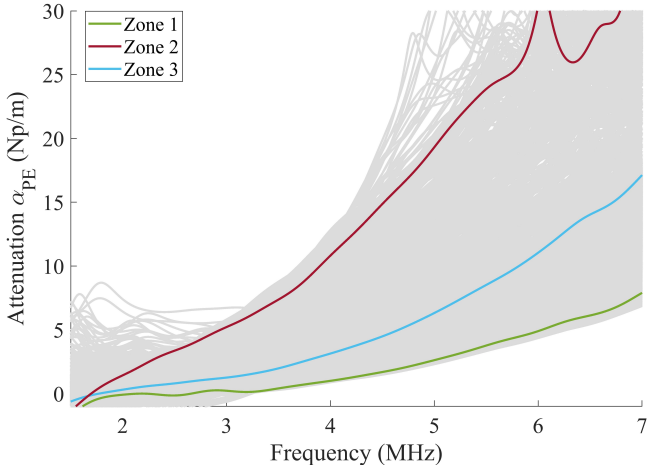

Figure 5: (Colour online) Attenuation at the centres of the three selected zones; gray lines represent the attenuation at all points within the rectangular area marked in Fig. 4(a).

fingerprinting procedure is necessary for parts too heavy to be manipulated directly under a microscope, but as a drawback may introduce stripe artefacts upon detaching the solidified fingerprint.

The contrast of the grain boundaries revealed to be too low to produce a binary image. The microscope scans were therefore printed in A3 format, and the boundaries were manually drawn upon a superimposed transparency film. This film was then scanned and the resulting image was fed into the processing workflow. Obviously, a more automated analysis would be highly desirable, in particular for larger sections for which the manual identification of grain boundaries quickly becomes tedious.

The scanned films for the three zones are shown in Fig. 6(a), (c) and (e). Each characterisation covered an area of approximately $1.35\,\text{mm} \times 0.96\,\text{mm}$. After binarisation, all images were processed to remove artefacts and close some open grain boundaries. The final step was the segmentation which yielded a numbered list of grains and their geometric properties, including size. All processing was done within *ImageJ* [28]. We assumed the standard definition of grain size, understood as the diameter of a circle of an area equal to that of the 2D grain in the metallographic image (equivalent diameter). The histograms of the equivalent diameters for the three zones are shown in Fig. 6(b), (d) and (f), together with the probability density functions of their log-normal fits. In this study, the Anderson-Darling test [29] was used to assess the quality of the fit. Comparing the diameters extracted from the metallography with multiple log-normal distributions, the best fit is the one which gives the maximum p-value, of which the definition can be found in [30]. The means and standard deviation-to-mean ratios of the fitted distributions are (51.9 µm, 0.74), (66.8 µm, 0.84) and (60.1 µm, 0.64) for Zone 1, Zone 2 and Zone 3, respectively.

3. FE modelling of ultrasound

To accompany and further elucidate the experimental examination of the mock-up, we used grain-scale finite element simulations of ultrasound. The models aimed at predicting the attenuation in the sample described in Section 2 and at investigating the effect of grain size distribution parameters on attenuation. Our numerical setup mimicked a plane wave scenario using a representative volume (cuboid) with prescribed grain size statistics and appropriate boundary conditions. The following sections introduce the details of the models used both in replicating the mock-up measurements and the parametric study reported in Section 4, and present the comparison between the predicted and measured attenuation. The FE models used throughout this paper built on tools and techniques we had established in previous work, for which we had demonstrated that the simulations are high-quality representations of the expected real behaviour of wave propagation and attenuation [12, 14, 18, 24, 31].

3.1. Details

Numerical synthetic microstructures were generated in *Neper* [32] using a log-normal distribution, which has been shown to be a realistic distribution of the grain size in metals [33, 34]. Based on the examination of the mock-up we chose the ranges of distribution parameters for investigation. The mean grain size, denoted by $\bar{D}$, and the standard deviation-to-mean ratio of the grain size, denoted by κ, ranged from 45 µm to 70 µm and from 0.2 to 0.6, respectively. For the sake of brevity, we describe a grain size distribution as $(\bar{D},\kappa)$. For example, a grain size distribution of (50 µm, 0.2) means that the mean grain size is 50 µm and the standard deviation is $0.2 \times 50\,\mu\text{m}{=}10\,\mu\text{m}$.

The geometry of each model was a cuboid, with the wave propagating in the direction of the longest side. The dimensions of the models were $(20\bar{D} \times 20\bar{D} \times 200\bar{D})$. After each model was generated, the Anderson-Darling test was conducted to test whether the grain size of the model followed the prescribed statistical distribution. All the tests failed to reject the null hypothesis at the default 1 % significance level, indicating that the grain sizes of all the generated models follow the prescribed distributions.

The models used regular structured meshes, which perform well with sufficiently fine discretisation in modelling a polycrystalline material [12]. We chose linear hexahedral elements (3D 8-node brick, of the C3D8 type) with an edge length of $\bar{D}/20$. All the models were composed of Inconel 600 with cubic symmetry. The elastic constants (C_{11},C_{12},C_{44}) and density of the crystal were (234.6 GPa, 145.4 GPa, 126.2 GPa) and $8290\,\text{kg/m}^3$, respectively.

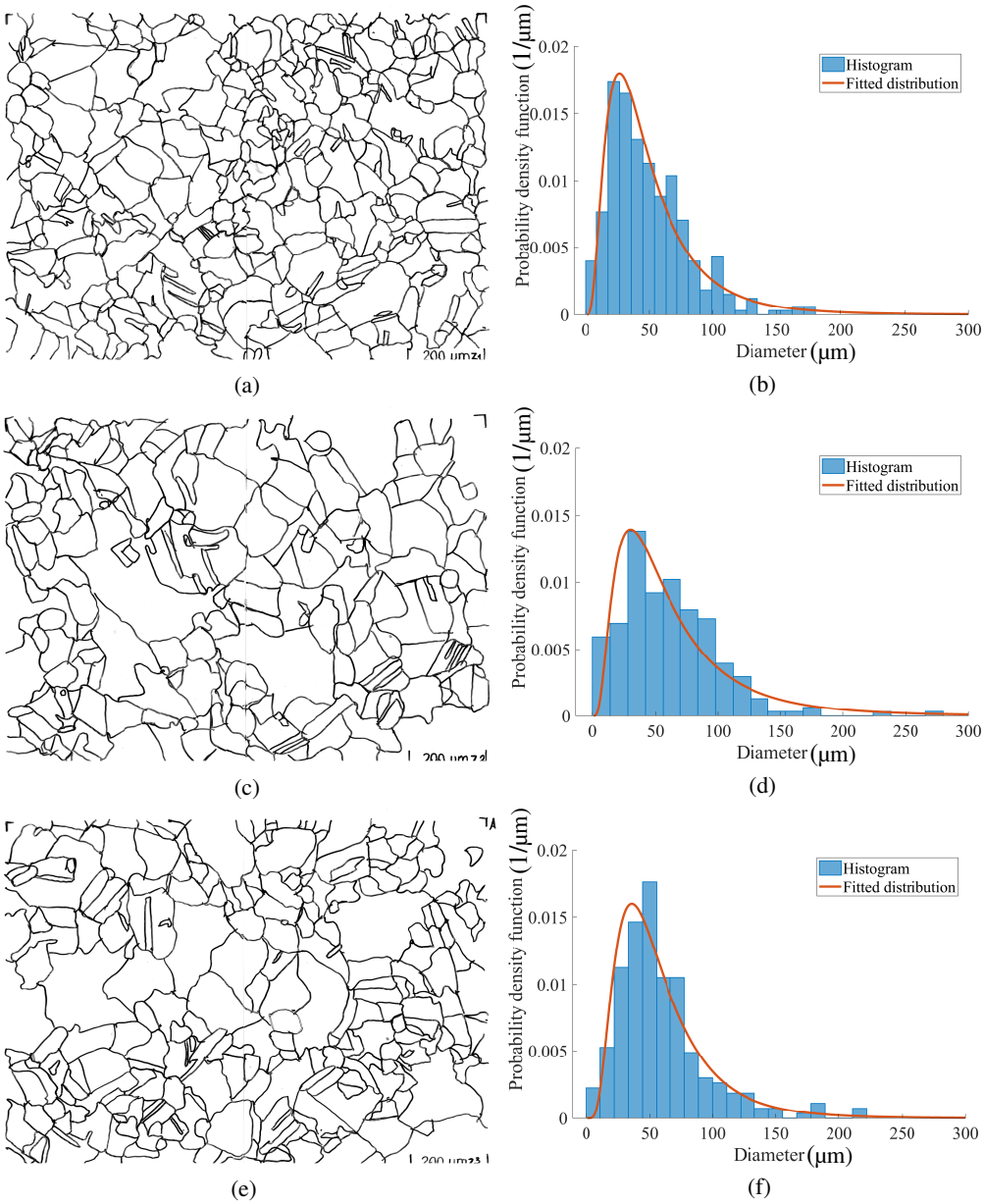

Figure 6: Metallographies of (a) Zone 1, (c) Zone 2 and (e) Zone 3, with histograms of the equivalent grain diameters and the probability density functions of their log-normal fits for: (b) Zone 1, (d) Zone 2 and (f) Zone 3.

To simulate the wave propagation, we used a highly efficient GPU-based FE solver Pogo [35]. A schematic diagram of the model used to calculate the attenuation is shown in Fig. 7. Symmetry boundary conditions used on the surfaces parallel to the $z-$axis made the model equivalent to being infinitely wide with repeating grain structures. All nodes on the $x-y$ plane, shown as the red dots in Fig. 7, acted as transmitters exciting a plane wave propagating in the $z-$direction. The nodes on the opposite surface, shown as the blue dots, acted as receivers. The coherent attenuation coefficient α was obtained by comparing the spatial average of the first wave packets received by the receivers to the spatial average of the responses over the transmitting nodes in the frequency domain. A 3-cycle Hann-windowed toneburst with centre frequencies of 6, 8, 10, 12 and 14 MHz was the excitation signal, covering the range from 6 to 14 MHz.

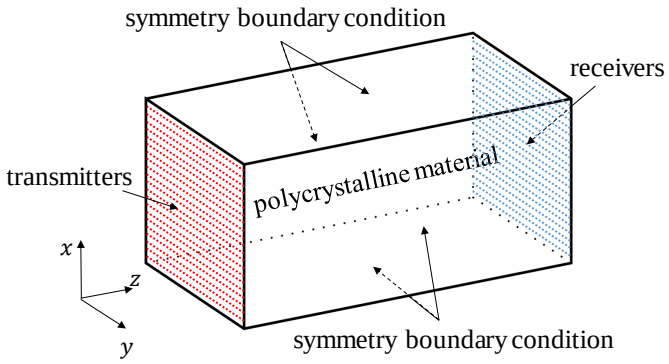

Figure 7: (Colour online) A schematic diagram of the model used for calculating attenuation.

In this paper, for each grain size distribution, one grain morphology is considered, with ten realisations of random orientations. A convergence study has been conducted to verify that the model dimensions, the element size and the number of realisations are sufficient, reported in Appendix A.

3.2. Comparison between the measured and simulated attenuation

In this section, we describe a 3D FE model generated using the statistics from the metallography image of the mock-up. The displacement time histories output from the model allow for predicting the attenuation which is then compared to the experimental result.

3.2.1. Microstructure reconstruction

The metallography measured at location 'Zone 1', of which the fitted log-normal distribution of equivalent diameters is (51.9 µm, 0.74), was used to reconstruct the microstructure. The relationship between the grain diameter distribution measured over a 2D surface and the volumetric statistics is complex and has not been explicitly expressed. Therefore, in this study, an iterative procedure was used to synthesise the 3D model. First, a microstructure was generated in *Neper* using the 2D fitted statistics. Then, the equivalent grain diameters were calculated from ten 2D uniformly spaced cross-sections, and the obtained distributions of diameters were fitted with log-normal distributions. If the cross-section distributions were sufficiently close to that obtained from the metallography, the generation procedure was complete. Otherwise, the inputs to *Neper*, i.e. the mean and standard deviation of the grain diameter, were adjusted.

Fig. 8 shows the distribution of the grain sizes used to generate the 3D model - (60 µm, 0.4), together with those calculated over the cross-sections and the 2D distribution calculated from the metallography. Good agreement is seen between the fitted distributions of the measurements from the metallograpy and from the cross-sections of the model, indicating the model is a good representation of the metallography. It can be seen that the standard deviation of the ten distributions measured at cross-sections is relatively small, indicating that the grain size distribution is relatively uniform throughout the model; this is different from the real sample where the grain size distribution is variable, as shown in Fig. 6(a), (c) and (e). Comparing the parameters of the log-normal fits of the 2D cross-sections and those of the 3D model, it can be seen that the 2D distribution shows a smaller mean but a larger variation; this is because the grains might not be sectioned through their centres and therefore exhibit smaller but more variable sizes.

3.2.2. FE model

The synthesised 3D microstructure was then used to build an FE model, which was meshed with hexahedral elements (3D 8-node brick element, C3D8) with an edge length of 5 µm. The material properties, boundary conditions, locations of transmitters and receivers were the same as those given in Section 3.1. The excitation was a 3-cycle Hann-windowed toneburst with a centre frequency of 6 MHz. The simulation of the FE model with 80 million elements was run by Pogo on two RTX 8000 GPU cards and the total execution time amounted to around 30 minutes.

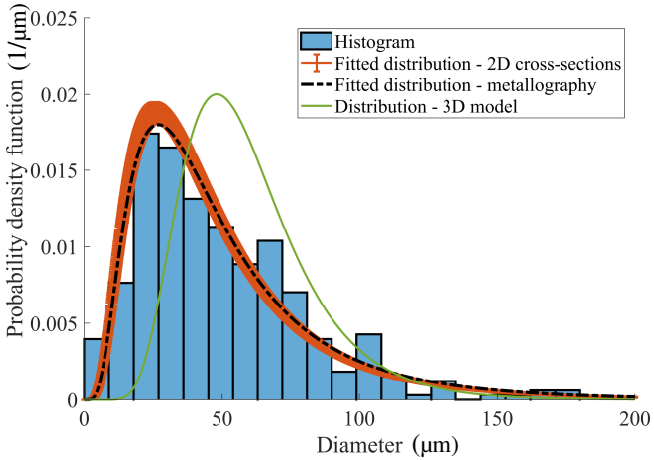

Figure 8: Probability density function of the fitted log-normal grain diameter distributions calculated from the metallography, the cross-sections (error bars show the standard deviation of the ten measurements) and the 3D model, together with the normalised histogram calculated from the metallography.

3.2.3. Results

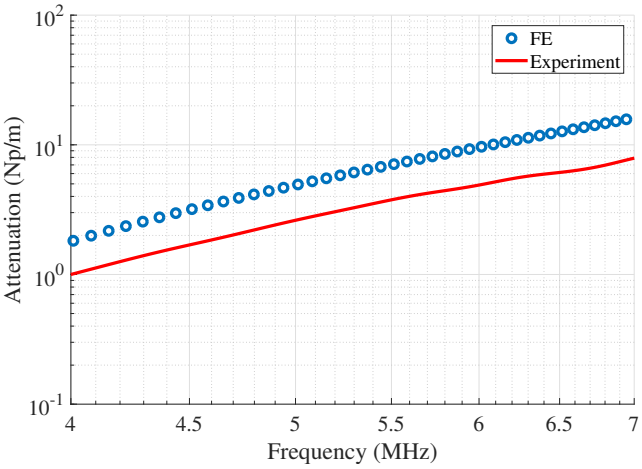

Figure 9: Comparison between the predicted and the experimentally measured attenuation.

The attenuation predicted with the FE model and averaged over ten realisations was compared with the experimental result measured at the centre of 'Zone 1' in Fig. 9. The FE prediction is about 1.8 times higher than the experimental measurement. This discrepancy may seem significant at first, but several remarks should be considered. First, the metallography fingerprint with dimensions of 1.26 mm × 0.91 mm is much smaller than the transducer area with a diameter of 9.53 mm. Hence, the grain statistics obtained from metallography may only partially describe the grains insonified by the transducer. Deviations of grain size, in particular the presence of large grains, even if small in number, can dominate the attenuation. In real life, its spatial variation, and hence the variation of the attenuation ranges, can be significant. With this perspective, the predicted results offer a good match and meet the typical expectations of the practitioners.

Second, the grain statistics could vary along the wave path of the inspection, the information which is not available from surface examination. Third, the examination procedure is prone to artefacts and some grain boundaries are ambiguous in the metallography image; in consequence, they may have been missed during

processing. This is expected to cause an overestimation in grain size, thereby resulting in an overestimated attenuation prediction. Finally, the FE model considers an idealised material, while in the real mock-up, some uncertainties, such as micro texture regions, might exist. We have conducted a study on the effect of the texture on attenuation, which is beyond the scope of this paper, and it indicated that adding texture to the considered microstructure changed the attenuation significantly. The impact of texture on attenuation has also been discussed by Lhuillier et al.[36].

4. Parametric study

In the previous sections, we presented the mock-up with spatially varying grain characteristics and the comparison between the measured and predicted attenuation for one location at the surface. The attenuation varied significantly across the surface, at a finer scale than the footprint of the transducer. In the inversion context, a thorough understanding of how the distribution affects the attenuation is essential. For a log-normal distribution, the mean and the standard deviation are two intuitive (and most commonly used in practice) descriptors. They can easily be obtained from a metallography image by appropriate processing. In this section, we discuss how the mean ($\bar{D}$) and standard deviation-to-mean ratio (κ) of the grain size distribution affect the attenuation and its dependence on frequency in a parametric study. Grain-scale time-domain FE simulation of ultrasound is used for the investigation.

The microstructures were generated in *Neper*, which takes the mean and standard deviation of a log-normal distribution as an optimisation target. We typically used around 5 million iterations to ensure convergence. The details of the models used in this section are listed in Tab. 1, where the mean and standard deviation-to-mean ratios of the grain size are calculated from the generated models. These parameters were very close to those prescribed as optimisation targets, so for simplicity, the prescribed values will be used hereafter. Tab. 1 shows that for a given mean grain size, the maximum grain size increases and the grain count decreases with the standard deviation-to-mean ratio. As the model dimensions are proportional to $\bar{D}$, the same grain count is seen for models with the same standard deviation-to-mean ratio.

4.1. The effect of the standard deviation-to-mean ratio

Attenuation against the standard deviation-to-mean ratio κ with different mean grain sizes: 50, 60 and 70 µm, at 10 MHz are plotted in Fig. 10. The figure indicates that the attenuation increases with κ in all the cases. As shown in Tab. 1, with increasing κ, the maximum grain size increases and the total grain count reduces; this causes an increase in the volume fraction of large grains, thereby resulting in the rise of attenuation. Fig. 10 also shows that the slope of the attenuation curve decreases with $\bar{D}$, as with larger mean grain size, the scattering shifts toward the stochastic region, where the attenuation is less sensitive to the grain size.

4.2. The effect of the mean grain size

In this section we focus on the effect of the mean grain size. Three standard deviation-to-mean ratios (0.2, 0.4 and 0.6) and for each ratio, mean grain size in the range of 45 to 70 µm were considered (grain counts for the models can be found in Tab. 1). From simulated time traces, we calculated the attenuation at 10 MHz for all combinations of grain size distributions. The results, plotted in Fig. 11 clearly indicate that the attenuation increases with mean grain size for all the cases, but less rapidly for models with a higher standard deviation-to-mean ratio.

With the help of power-law fitting, we estimated the dependence of attenuation on the mean grain size, which is listed in the third column of Tab. 2. The power reduces from 2.62 to 1.38 when increasing κ from 0.2 to 0.6. The minimum wavelength to mean grain size ratio is 8.6; this ratio is much greater than 1, suggesting the scattering is in the Rayleigh regime (Eq. (1)). However, as illustrated in the previous section, increasing the standard deviation-to-mean ratio allows larger grains to appear, and shifts the scattering towards the stochastic region, causing a power drop in the mean grain size dependence. For comparison, we repeated the same calculation at 6 and 14 MHz and included the results in Tab. 2. For both frequencies, a similar trend, i.e. a lower power for a higher κ, is observed.

Table 1: Grain size information for the numerical microstructures used in this study; mean and standard deviation (std) are calculated from the generated models.

mean diameter(µm)	std of diameter (µm)	ratio	maximum diameter(µm)	grain count
45	9	0.2	102.4	135, 829
45	18.1	0.4	169.9	97, 885
45.3	27.4	0.6	241.8	60, 912
50	10	0.2	119.6	135, 829
50	15	0.3	163.3	117, 981
50	20.1	0.4	182.8	97, 885
50.2	25.2	0.5	216.6	78.236
50.3	30.5	0.6	260.1	60, 912
55	11	0.2	124.9	135, 829
55	22.1	0.4	206.4	97, 885
55.2	33.3	0.6	308.7	60, 912
60	12	0.2	135	135, 829
60	18.1	0.3	196.4	117, 981
60	24.1	0.4	222	97, 885
60.2	30.2	0.5	267.6	78, 236
60.3	36.5	0.6	323.3	60, 912
65	13	0.2	147.1	135, 829
65.1	26.1	0.4	239.9	97, 885
65.5	39.8	0.6	344	60, 912
70	14.1	0.2	198.8	135, 829
70	21	0.3	234.3	117, 981
70.1	28.2	0.4	256.5	97, 885
70.2	35.3	0.5	331.6	78, 236
70.4	42.6	0.6	369.2	60, 912

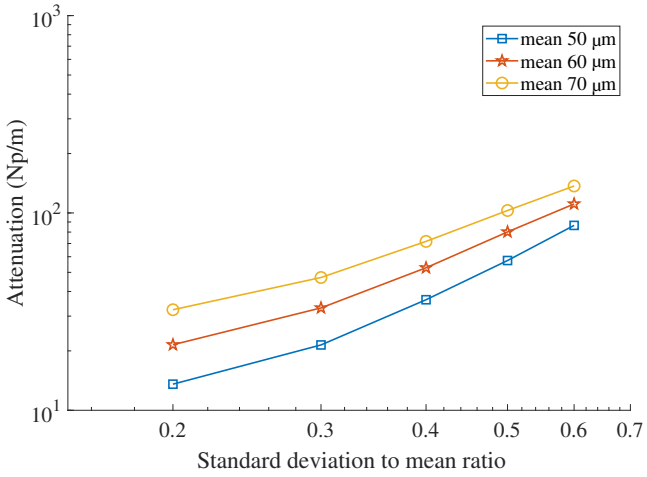

Figure 10: Attenuation against the standard deviation-to-mean ratio at 10 MHz with different mean grain sizes.

Table 2: Fitted exponent of the power-law relationship between attenuation and mean grain size; std stands for standard deviation.

std to mean ratio	frequency 6 MHz	frequency 10 MHz	frequency 14 MHz
0.2	3.17	2.62	2.26
0.4	2.68	2.04	1.69
0.6	2.14	1.38	1.31

Tab. 2 also shows that the exponent of the power-law relationship between attenuation and mean grain size reduces with frequency. This can also be seen in Fig. 12, which shows that the attenuation against mean grain size curve increases less rapidly for a higher frequency. This is because the wavelength becomes shorter with the increasing frequency, which shifts the scattering to the stochastic regime.

4.3. The effect of the distribution parameters on the frequency dependence

In this section, we demonstrate how the distribution parameters affect the frequency dependence of attenuation. Models with a mean grain size of 50 μm and standard deviation-to-mean ratios ranging from 0.2 to 0.6 are considered. As before, the grain count for each model can be found in Tab. 1. We simulated the ultrasound with centre frequencies from 6 MHz to 14 MHz, so that the minimum wavelength-to-mean grain size ratio was 8.6, significantly greater than 1. According to Eq. (1), this indicates that the scattering is in the Rayleigh regime and the fourth power frequency dependence is expected for attenuation.

Attenuation against frequency curves with different standard deviation-to-mean ratios of grain size are plotted in Fig. 13. The attenuation increases with frequency for all cases, but less rapidly for larger standard deviation-to-mean ratios. The fitted power of the frequency dependence of attenuation is listed in Tab. 3. Two frequency ranges, 6–7 MHz and 13–14 MHz, are used for fitting each of the five curves corresponding to different standard deviation-to-mean ratios. Tab. 3 shows that, when increasing κ from 0.2 to 0.6, the power of frequency dependence reduces from 4.13 to 3.09 over the frequency range of 6–7 MHz, and from 3.56 to 2.06 over the frequency range of 13–14 MHz. It is worth noting that the power 4.13, which is larger than 4, could be due to the coarse element used for calculation, shown in Fig. A.2 in Appendix A. At a higher frequency, the power drops more rapidly. The decrease of the power of frequency dependence indicates that the scattering is out of the Rayleigh region, although the wavelength-to-mean grain size ratio is much greater than 1.

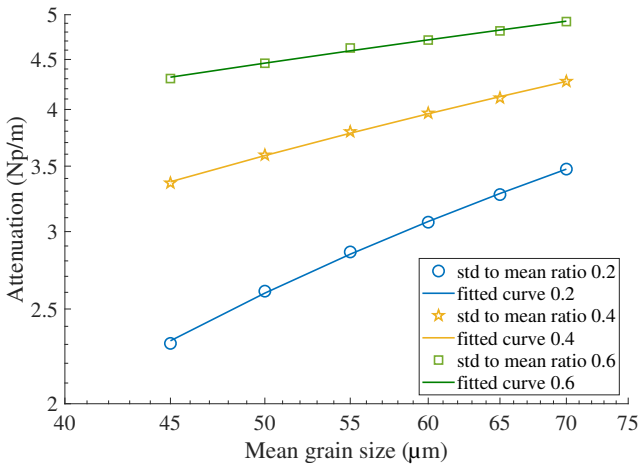

Figure 11: Attenuation vs mean grain size obtained with the models with standard deviation-to-mean ratios of 0.2, 0.4 and 0.6, at 10 MHz; std stands for standard deviation.

Table 3: Fitted power of frequency dependence of attenuation; std stands for standard deviation.

mean (μm)	std (μm)	std to mean ratio	fitted power (6–7 MHz)	fitted power (13–14 MHz)
50	10	0.2	4.13	3.56
50	15	0.3	3.45	3.27
50	20	0.4	3.56	2.98
50	25	0.5	3.42	2.71
50	30	0.6	3.09	2.06

As shown in Tab. 1, with a high standard deviation-to-mean ratio, the maximum grain size can be much larger that $\bar{D}$. With a mean grain size of 50 μm, a standard deviation-to-mean ratio of 0.6 and a frequency of 14 MHz, the wavelength-to-grain size can be as low as 1.6. According to Eq. (1), at this ratio, the scattering is in the stochastic region and the attenuation is proportional to frequency squared. This explains why the power of frequency dependence drops significantly with standard deviation-to-mean ratio.

We showed that increasing standard deviation-to-mean ratio of the grain size increases the volume fraction of large grains and thus makes the scattering shift to the stochastic region. Similar trend is expected when increasing $\bar{D}$. Fig. 14 shows the frequency dependence of attenuation for different mean grain sizes at a constant κ of 0.4. Comparing Fig. 13 and Fig. 14, suggests that the attenuation varies more significantly when changing κ from 0.2 to 0.6 than when increasing $\bar{D}$ from 45 μm to 70 μm.

4.4. Non-uniqueness of the grain size distribution

The results in the previous subsections showed that increasing the mean and standard deviation-to-mean ratio of the grain diameter both increase the attenuation and decrease the frequency dependence power of attenuation. Therefore, there is a possibility that two distributions, one with a large mean and small standard deviation-to-mean ratio and the other one with a small mean and large standard deviation-to-mean ratio, have similar attenuation against frequency curves. We demonstrate such a scenario in Fig. 15, which shows two sets of examples. The models with distributions of (45 μm, 0.6) and (70 μm, 0.4) have very similar attenuation curves, higher than the other set of examples of (50 μm, 0.3) and (60 μm, 0.2), which are also very close to each other. This highlights a big challenge for determining mean grain size from an ultrasonic attenuation measurement.

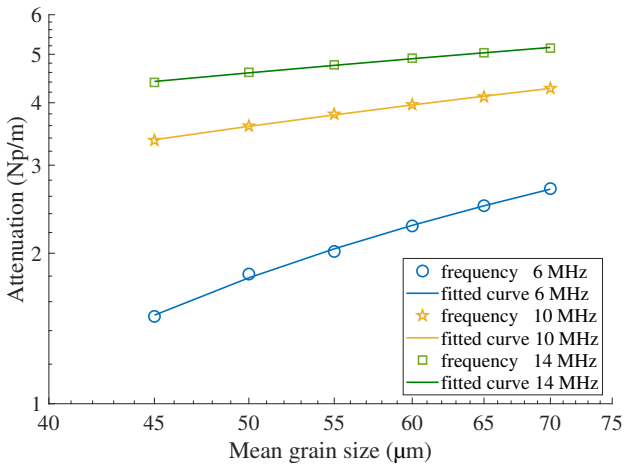

Figure 12: Attenuation vs mean grain size obtained with the models with a standard deviation-to-mean ratio of 0.4, at 6, 10 and 14 MHz.

The TPCFs for both pairs of curves in Fig. 15 are plotted in Fig. 16. As expected, the TPCFs of the models which have similar attenuation curves overlap too, even if their mean and standard deviation-to-mean ratio of the grain diameter are very different. Hence, it is clear that unlike $\bar{D}$, the linear correlation length can be estimated unambiguously from the TPCF. While this measure is less commonly used in industry, it may serve as a more robust 'single value' description of grain morphology for components of industrial relevance. The unquestionable advantage of this description is that it can be directly linked to established theoretical models for polycrystalline materials.

5. Grain size estimation from attenuation measurement

As mentioned in Section 1, one aim of this study was to elucidate the limitations of grain size estimation based on attenuation measurement, which is discussed in this section. We employ the second-order approximation [17], which uses a TPCF to describe the grain statistics, to predict the attenuation. As mentioned in Section 1, the TPCF is often modelled by an exponential function, $\exp(-r/a)$, where a is the linear correlation length. While average grain size is the most common metric used in the industry, in this section we consider the linear correlation length as the target for the inverse problem.

Three attenuation curves, measured at the centres of the different locations, 'Zone 1', 'Zone 2' and 'Zone 3', were used to evaluate the grain size. Locations of the three zones can be found in Fig. 4. A family of theoretical curves were first produced using the second-order approximation model with a set of linear correlation lengths. Then, the attenuation measurements were compared with the theoretical curves. The correlation length offering the best match was identified as the target value characterising the microstructure at each location. The values identified from the attenuation measurement were compared with the correlation lengths obtained by fitting single exponentials to the TPCFs calculated from the metallography images shown in Fig. 6.

The comparison of the linear correlation lengths calculated from the metallography images and estimated from the attenuation measurements is gathered in Tab. 4. Zone 1 and Zone 3 show good agreement, with the evaluation from ultrasonic measurements being 10-20 % lower than the metrics obtained from metallography. Possible reasons for the small discrepancy between them are similar to those listed in Section 3.2.3, with the variability of the microstructure along the wave path supposed to have the strongest effect.

However, the comparison of Zone 2 shows a larger discrepancy, and the trend is opposite to the others, i.e. the estimation from attenuation is higher than the reference from the metallography image. This different trend may be explained by Fig. 17 and Fig. 4(a), which show the measured TPCFs and fitted TPCFs for the

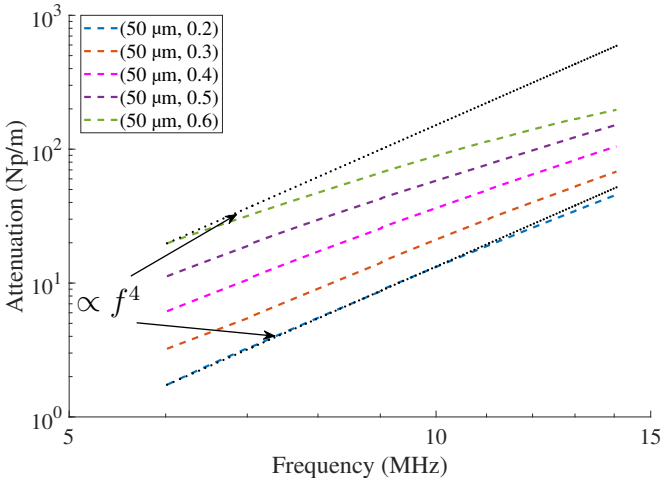

Figure 13: (Colour online) Frequency dependence of attenuation obtained with a mean grain size of 50 µm and standard deviation-to-mean ratios from 0.2 to 0.6.

Table 4: Linear correlation lengths calculated from the metallography images and estimated from the attenuation measurements.

zone number	from metallography	from attenuation	relative error %
Zone 1	33.6	27.8	17
Zone 2	47.6	66.7	−40
Zone 3	45.0	38.8	14

three zones and the attenuation measured across the mock-up at 5 MHz, respectively. It can be seen that, for Zone 2, a single exponential which gives the best fit underestimates the fraction of large grains, which dominate the attenuation. On the other hand, for the other zones, there is a relatively good agreement between the measured and the fitted TPCFs. In addition, Fig. 4(a) suggests that the grain size distribution is relatively uniform near Zone 1 and Zone 3 but it varies considerably around Zone 2. The bright yellow spot near Zone 2 represents a high attenuation and suggests there are large grains in that area. Therefore, the small metallography fingerprint taken in Zone 2 might not be able to reflect the microstructure seen by the transducer. Hence, the linear correlation length obtained from the metallography very likely underestimates the grain size. We also note that our work assumes equiaxed grains which may not always be satisfied, in particular close to the edges. Although there is no evidence that columnar grains or texture are present in this sample, they remain a factor to consider when using the method presented in the paper.

Such a difficulty can only be resolved by reducing the transducer footprint which is often not practical. Nevertheless, we can conclude with confidence that if the grain size distribution is relatively uniform near the zone of the inspection, good estimation of the linear correlation length can be obtained using the attenuation measurement. In fact, the discrepancies presented in Tab. 4 seem insignificant in a practical context where, for instance, a qualification for a certain inspection protocol is desired. A key factor here is the use of the linear correlation length as the grain size descriptor which provides a unique representation unlike, perhaps more intuitive, grain size distribution. Unfortunately, the single exponential fit has its limitations – we noted that it performed very well only for Zone 1. More complex microstructures would require more complex forms of TPCF, for instance multi-exponential. However, we believe that even such a simplified fit can deliver a useful, 'single-number' metric to characterise castings for inspection qualification.

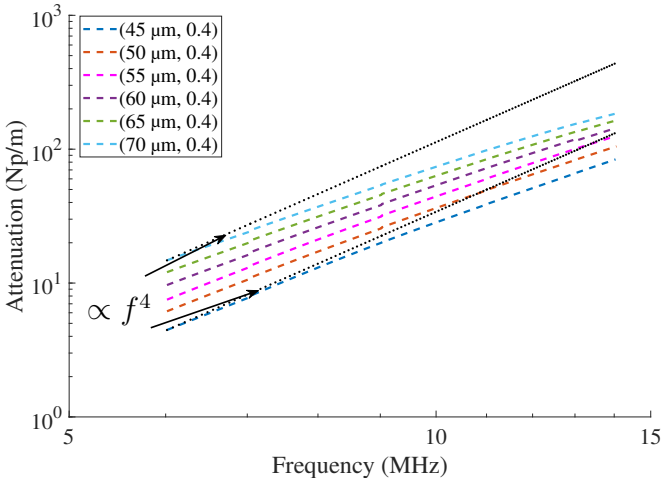

Figure 14: (Colour online) Frequency dependence of attenuation obtained with a standard deviation-to-mean ratio of 0.4 and mean grain sizes from 45 to 70 µm.

6. Conclusions

Inspired by an industrial cast alloy mock-up with spatially varying grain properties, this study investigated how the statistical distribution of grain size affects the attenuation of ultrasound. We combined experimental measurements of attenuation and metallography examinations of several zones on the mock-up surface with grain-scale finite element simulations of ultrasound to elucidate the potential and limitations of using the attenuation measurement for assessing the inspectability of the components using a given qualified procedure.

A grain-scale 3D FE model was generated based on the grain size statistics obtained from the metallography image. A comparison between the FE prediction of attenuation and the experimental measurement showed a discrepancy. While it seemed significant at first, we suggested several potential reasons for consideration, one of which being the spatial variation of grain characteristics. The parametric study, which followed, identified the relationships between the parameters of the log-normal distribution and the attenuation.

Increasing the mean or the standard deviation-to-mean ratio of grain diameter both were shown to elevate attenuation and reduce the power of frequency dependence as the scattering shifted towards the stochastic regime. Owing to the similar trends caused for both the mean and standard deviation-to-mean ratio, structures with different grain size distributions could result in similar attenuation. Having demonstrated this effect numerically, we suggested that the linear correlation length is a more appropriate and robust measure, not affected by the non-uniqueness.

In the final section, we used the second-order approximation to estimate the linear correlation length from attenuation measurements. The predictions were compared to those calculated from metallography. We found the estimation to be within 10-20 % of the benchmark for cases with a relatively constant grain size statistics near the zone of the inspection. When the spatial variation of the statistical parameters was large, the error of the inversion doubled. Acknowledging the limitations of a single exponential fit to the TPCF, we concluded that the linear correlation length is a promising metric describing grain size statistics which could be used for qualification for inspection. Its advantages include the direct relevance to established attenuation models and that it can be determined from the attenuation measurement within satisfactory confidence.

The linear correlation length presented in this paper was suggested as a metric to quantify to what extent the microstructure of a component under inspection is similar to the microstructure of the mock-ups on which the inspection method was qualified. If the microstructure of the actual component under inspection exhibits a larger average grain size, a degradation of the inspection performance would be expected. On the other

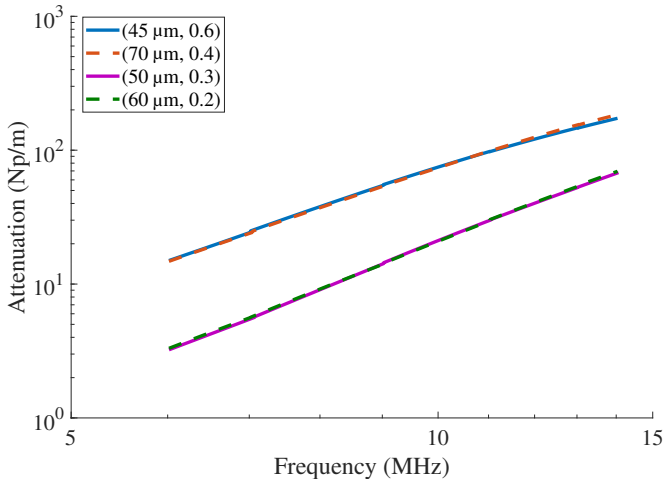

Figure 15: (Colour online) Examples of similar attenuation curves obtained with different grain size distributions.

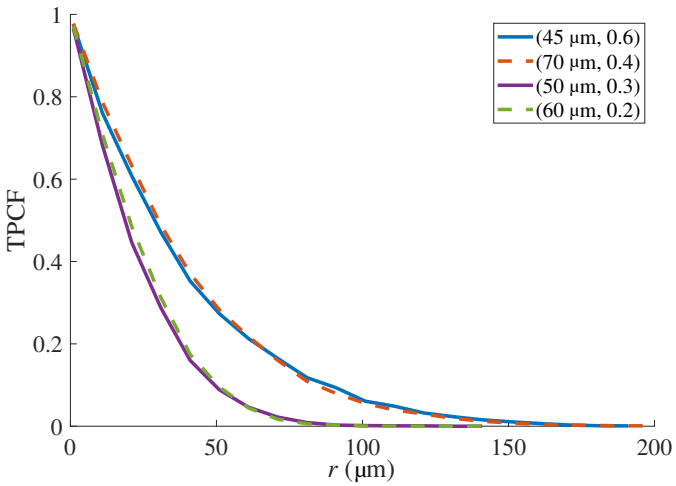

Figure 16: (Colour online) TPCFs of different grain size distributions.

hand, a smaller average grain size should increase the performance margin. With this in mind, a logical next step would be to apply the linear correlation length metric to an actual cast component mock-up in order to produce an extended cartography covering the entire inspection surface. One might expect to find more significant local grain size variations in a component mock-up, which the linear correlation length cartography should reflect. Implanting defects on regions identified as penalising due to a coarser grain structure should then allow to determine the actual inspection performance degradation, and to establish acceptable margins.

Acknowledgement

This project has received funding from the Euratom research and training programme 2014-2018 under grant agreement No 755500 (ADVISE – www.advise-h2020.eu).

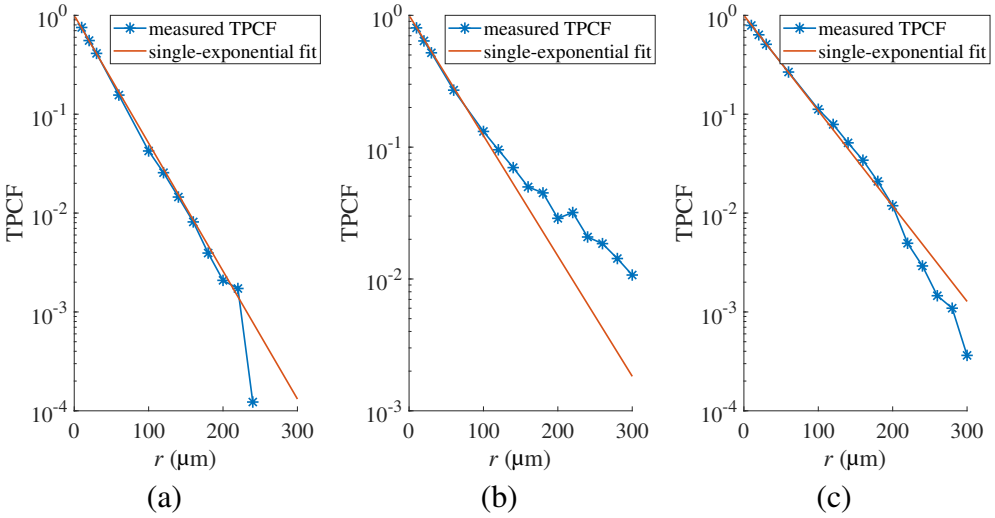

Figure 17: Measured TPCFs of (a) Zone 1, (b) Zone 2 and (c) Zone 3 and their single-exponential fits.

Appendix A. FE model convergence

This appendix reports the convergence study which preceded simulations. We verify whether the dimensions of the model and the element size given in Section 3.1 are sufficient and whether the number of realisations for each distribution enables an accurate representation to be obtained.

Dimensions

Using the symmetry boundary condition, an infinitely wide model is achieved by repeating the grain structures; this enlarges the grains on the boundaries where the condition is applied. If the initial model is not sufficiently wide, the boundary effect can alter the grain size distribution of the equivalent infinite model from the prescribed distribution [18]. To test whether the width of the model is sufficient to remove the boundary effect, attenuation predicted by models with the same depth but different cross-sectional areas were compared. Apparently, the size of a model consisting of fine grains can be relatively small compared to its counterpart with large grains. Therefore, the model size should be related to the grain size. Because the width of the model was proportional to $\bar{D}$, only the convergence of the models with a mean grain size of 50 µm were assessed and the models with the other mean grain sizes were expected to behave similarly in terms of the convergence. Two models with the minimum and maximum standard deviation-to-mean ratios discussed in this study, 0.2 and 0.6, were considered. Fig. A.1 shows the attenuation predicted by the models with the cross-sectional areas of $(20\bar{D}, 20\bar{D})$, $(22\bar{D}, 22\bar{D})$ and $(24\bar{D}, 24\bar{D})$. For the model with a distribution of (50 µm, 0.2), the root-mean-square (RMS) of the relative discrepancy at all frequencies is 2.21 % and for the other one with a κ of 0.6, it is 1.77 %. Therefore, enlarging the cross-sectional area from $(20\bar{D}, 20\bar{D})$ to $(24\bar{D}, 24\bar{D})$ has a minor effect on attenuation and given the practical context of this study, such a precision was considered acceptable.

Element size

The element size in simulation of ultrasound in polycrystals is typically determined by the wavelength and the grain size [12]. With the highest frequency discussed in this study, 14 MHz, there are at least 20 elements per wavelength for all models, which fulfils the wavelength criterion [12].

To test whether the element is sufficiently fine to represent the grains' behaviour, models with different element sizes were compared. Because the element size is proportional to $\bar{D}$, the convergence of two models with grain size distributions of (50 µm, 0.2) and (50 µm, 0.6) was assessed. The models were both meshed

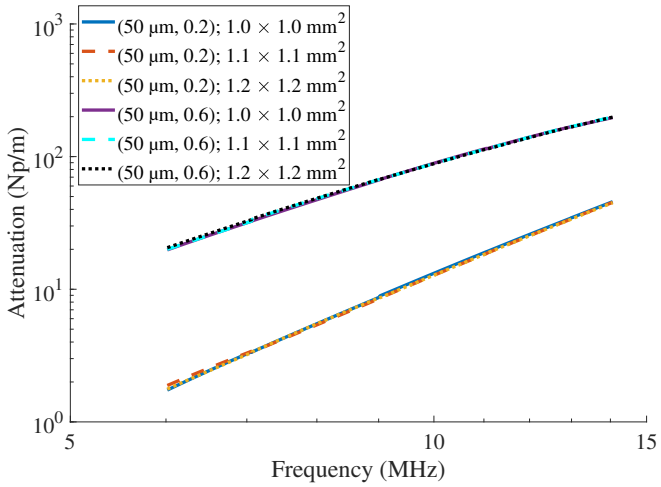

Figure A.1: (Colour online) Attenuation predicted by models with different cross-sectional areas.

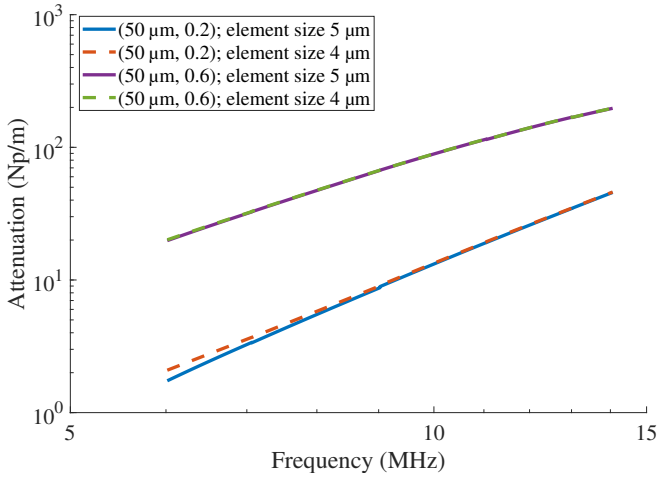

Figure A.2: (Colour online) Attenuation predicted by models with different element sizes.

with element edge lengths of 5 µm and 4 µm and their associated attenuation results are compared in Fig. A.2. A deviation can be observed with the (50 µm, 0.2) case at low frequencies where the small attenuation (on the order of 0.01 Np) exerts a magnification effect on the improvement of numerical accuracy as caused by mesh refinement [18]. The discrepancy tends to decrease with increasing frequency and becomes minor beyond around 9 MHz. The overall RMS of the relative discrepancy is 6.14 %. For the other distribution, good agreement can be seen at all the inspection frequencies, with a relative RMS error of 0.44 %. As demonstrated in Section 4, with an increasing standard deviation-to-mean ratio, the volume fraction of large grains, which dominate the attenuation behaviour, increases. Therefore, good agreement can be obtained with a large standard deviation-to-mean ratio but not with a small one. Using finer meshing significantly increases computational cost, and the error induced by the coarse mesh has an obvious effect on the attenuation only when the standard deviation-to-mean ratio of the grain size and inspection frequency are both low. Therefore, as a compromise, the element size is kept at $\bar{D}/20$.

Realisations

To obtain statistically relevant characteristics of a given grain size distribution, one needs to consider a number of random models. Previous work showed that for Poisson-Voronoi distributions, it is sufficient to reshuffle random grain orientations without changing grain morphology, which greatly reduces the computational burden [12]. In this section, we verify whether this also holds for a log-normal distribution of grain size and determine the number of realisations which ensures that the results are within satisfactory confidence bounds.

It is expected that a model with more grains needs fewer realisations to yield representative statistics. Because the dimensions of a model are proportional to $\bar{D}$s, the models with different mean grain sizes but the same standard deviation-to-mean ratios contain the same number of grains, as shown in Tab. 1. Analogously to the previous convergence studies, two grain size distributions (50 µm, 0.2) and (50 µm, 0.6) are considered. The frequency is 10 MHz for the following convergence study.

First, we establish how many realisations, obtained by reshuffling random crystallographic orientations, are sufficient to obtain convergence. We considered three different morphological structures for both distributions (six structures in total, denoted by S1 to S6 in Fig. A.3), and simulated ultrasound over fifty realisations for each model. Fig. A.3 shows the average attenuation against the number of realisations used for averaging, normalised by the average attenuation using all the fifty realisations for each model. Error bars show the standard error of the mean, i.e. the ratio of the standard deviation to the square root of the number of the realisations, also normalised in the same manner as the mean. It can be seen that after ten realisations, the normalised attenuation varies within a range of ±5% for all cases, which is accepted as a convergence limit in this study.

Second, we verify whether one morphological structure with ten realisations of random orientations is sufficient to obtain a statistically representative attenuation. For each distribution, ten structures with different grain morphologies were generated and for each structure, ten realisations of random crystallographic orientations were executed – in total a hundred of realisations. Fig. A.4 shows how the average attenuation, shown as the curves, and the standard error of the mean, shown as the error bars, change with the number of structures used for averaging, normalised by the average attenuation using all the ten structures. It is worth noting that the number of the realisations are ten times that of the structure, therefore when the number of structure is one, the point and error bar show the mean and the standard error of the mean of the ten realisations of random orientations. It can be seen that the normalised attenuation obtained using one morphological structure varies within a small range of ±5%, indicating that to obtain statistically relevant results for a log-normal distribution it is sufficient to reshuffle material orientation assignments (with ten realisations) using a single grain geometry.

References

[1] W. P. Mason, H. McSkimin, Attenuation and scattering of high frequency sound waves in metals and glasses, The Journal of the Acoustical Society of America 19 (1947) 464–473.

[2] H. Huntington, On ultrasonic scattering by polycrystals, The Journal of the Acoustical Society of America 22 (1950) 362–364.

[3] W. Roth, Scattering of ultrasonic radiation in polycrystalline metals, Journal of Applied Physics 19 (1948) 901–910.

[4] W. Mason, H. McSkimin, Energy losses of sound waves in metals due to scattering and diffusion, Journal of Applied Physics 19 (1948) 940–946.

[5] R. K. Roney, The influence of metal grain structure on the attenuation of an ultrasonic acoustic wave, Ph.D. thesis, California Institute of Technology (1950).

[6] R. Smith, The effect of grain size distribution on the frequency dependence of the ultrasonic attenuation in polycrystalline materials, Ultrasonics 20 (1982) 211–214.

[7] D. Nicoletti, A. Anderson, Determination of grain-size distribution from ultrasonic attenuation: transformation and inversion, The Journal of the Acoustical Society of America 101 (1997) 686–689.

[8] F. E. Stanke, G. Kino, A unified theory for elastic wave propagation in polycrystalline materials, The Journal of the Acoustical Society of America 75 (1984) 665–681.

[9] R. L. Weaver, Diffusivity of ultrasound in polycrystals, Journal of the Mechanics and Physics of Solids 38 (1990) 55–86.

[10] F. E. Stanke, Spatial autocorrelation functions for calculations of effective propagation constants in polycrystalline materials, The Journal of the Acoustical Society of America 80 (1986) 1479–1485.

[11] C.-S. Man, R. Paroni, Y. Xiang, E. A. Kenik, On the geometric autocorrelation function of polycrystalline materials, Journal of Computational and Applied Mathematics 190 (2006) 200–210.

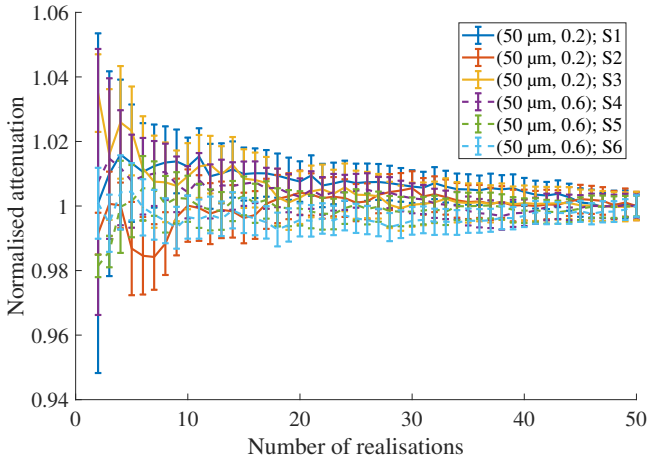

Figure A.3: (Colour online) Average attenuation at 10 MHz against the number of realisations used for averaging, normalised by the average attenuation using all the fifty realisations for each structure. Error bars show the standard error of the mean, i.e. the ratio of the standard deviation to the square root of the number of the realisations, also normalised in the same manner as the mean. Six structures are denoted by S1 to S6, with S1, S2 and S3 for (50 µm, 0.2) and S4, S5 and S6 for (50 µm, 0.6).

[12] A. Van Pamel, G. Sha, S. I. Rokhlin, M. J. S. Lowe, Finite-element modelling of elastic wave propagation and scattering within heterogeneous media, Proceedings of the Royal Society A: Mathematical, Physical and Engineering Sciences 473 (2017) 20160738.

[13] M. Ryzy, T. Grabec, P. Sedlák, I. A. Veres, Influence of grain morphology on ultrasonic wave attenuation in polycrystalline media with statistically equiaxed grains, The Journal of the Acoustical Society of America 143 (2018) 219–229.

[14] A. Van Pamel, G. Sha, M. J. S. Lowe, S. I. Rokhlin, Numerical and analytic modelling of elastodynamic scattering within polycrystalline materials, The Journal of the Acoustical Society of America 143 (2018) 2394–2408.

[15] M. Norouzian, J. A. Turner, Ultrasonic wave propagation predictions for polycrystalline materials using three-dimensional synthetic microstructures: Attenuation, The Journal of the Acoustical Society of America 145 (2019) 2181–2191.

[16] M. Norouzian, S. Islam, J. A. Turner, Influence of microstructural grain-size distribution on ultrasonic scattering, Ultrasonics 102 (2020) 106032.

[17] G. Sha, M. Huang, M. Lowe, S. Rokhlin, Attenuation and velocity of elastic waves in polycrystals with generally anisotropic grains: Analytic and numerical modeling, The Journal of the Acoustical Society of America 147 (2020) 2442–2465.

[18] M. Huang, G. Sha, P. Huthwaite, S. Rokhlin, M. Lowe, Maximizing the accuracy of finite element simulation of elastic wave propagation in polycrystals, The Journal of the Acoustical Society of America 148 (2020) 1890–1910.

[19] A. P. Arguelles, J. A. Turner, Ultrasonic attenuation of polycrystalline materials with a distribution of grain sizes, The Journal of the Acoustical Society of America 141 (2017) 4347–4353.

[20] G. Sha, Analytical attenuation and scattering models for polycrystals with uniform equiaxed grains, The Journal of the Acoustical Society of America 143 (2018) EL347–EL353.

[21] G. Sha, Correlation of elastic wave attenuation and scattering with volumetric grain size distribution for polycrystals of statistically equiaxed grains, Wave Motion 83 (2018) 102–110.

[22] M. A. Groeber, M. A. Jackson, Dream. 3d: a digital representation environment for the analysis of microstructure in 3d, Integrating materials and manufacturing innovation 3 (2014) 5.

[23] X. Bai, Y. Zhao, J. Ma, Y. Liu, Q. Wang, Grain-size distribution effects on the attenuation of laser-generated ultrasound in α-titanium alloy, Materials 12 (2019) 102.

[24] A. Van Pamel, C. R. Brett, P. Huthwaite, M. J. S. Lowe, Finite element modelling of elastic wave scattering within a polycrystalline material in two and three dimensions, The Journal of the Acoustical Society of America 138 (2015) 2326–2336.

[25] Y. Liu, A. Van Pamel, P. B. Nagy, P. Cawley, Investigation of ultrasonic backscatter using three-dimensional finite element simulations, The Journal of the Acoustical Society of America 145 (2019) 1584–1595.

[26] P. He, J. Zheng, Acoustic dispersion and attenuation measurement using both transmitted and reflected pulses, Ultrasonics 39 (2001) 27–32.

[27] P. H. Rogers, A. L. Van Buren, An exact expression for the lommel-diffraction correction integral, The Journal of the Acoustical Society of America 55 (1974) 724–728.

[28] J. Schindelin, I. Arganda-Carreras, E. Frise, V. Kaynig, M. Longair, T. Pietzsch, S. Preibisch, C. Rueden, S. Saalfeld, B. Schmid, et al., Fiji: an open-source platform for biological-image analysis, Nature methods 9 (2012) 676–682.

[29] T. W. Anderson, D. A. Darling, A test of goodness of fit, Journal of the American Statistical Association 49 (1954) 765–769.

[30] M. John, A dictionary of epidemiology, Oxford university press, 2001.

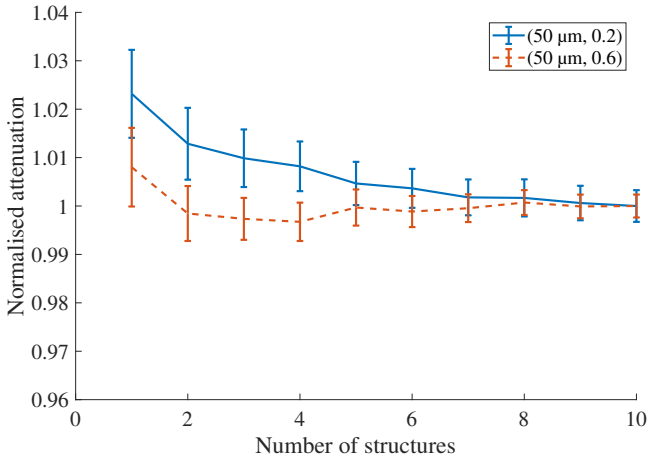

Figure A.4: Average attenuation, shown as the curves, and the standard error of the mean, shown as the error bars, against the number of structures used for averaging, normalised by the average attenuation using all the ten structures. For each structure, ten realisations of random orientations were executed, so the number of the realisations are ten times that of the structure, i.e. when the number of structure is one, the point and error bar show the mean and the standard error of the mean of the ten realisations of random orientations.

[31] A. Van Pamel, P. B. Nagy, M. J. Lowe, On the dimensionality of elastic wave scattering within heterogeneous media, The Journal of the Acoustical Society of America 140 (2016) 4360–4366.

[32] R. Quey, P. R. Dawson, F. Barbe, Large-scale 3D random polycrystals for the finite element method: Generation, meshing and remeshing, Computer Methods in Applied Mechanics and Engineering 200 (2011) 1729–1745.

[33] E. P. Papadakis, From micrograph to grain-size distribution with ultrasonic applications, Journal of Applied Physics 35 (1964) 1586–1594.

[34] J. J. Bucki, K. J. Kurzydłowski, Analysis of the effect of grain size uniformity on the flow stress of polycrystals: Part I: Studies of the relationship between the variance of grain volume and the variance of the grain area on polycrystal cross section, Materials Characterization 29 (1992) 365–374.

[35] P. Huthwaite, Accelerated finite element elastodynamic simulations using the GPU, Journal of Computational Physics 257 (2014) 687–707.

[36] P. Lhuillier, B. Chassignole, M. Oudaa, S. Kerhervé, F. Rupin, T. Fouquet, Investigation of the ultrasonic attenuation in anisotropic weld materials with finite element modeling and grain-scale material description, Ultrasonics 78 (2017) 40–50.